Volume 1 | Number 1 | Jan 2013 | Pages 1–100

NJC

New Journal of Chemistry

www.rsc.org/njc

A journal for new directions in chemistry

ROYAL SOCIETY OF CHEMISTRY

Journal Name RSCPublishing

ARTICLE

Cite this: DOI: 10.1039/x0xx00000x

Received 00th January 2012,
Accepted 00th January 2012

DOI: 10.1039/x0xx00000x

www.rsc.org/

Functionalization of Carbon Nanotubes via the Birch Reduction Chemistry for Selectively Loading of CuO Nanosheets

Huiting Sun, [a] Xiaoping Song, [a] Minwei Xu,* [a, b] Yin Zhang, [a] Wenxiu Que [b] and Sen Yang * [a]

Mesoporous CuO nanosheets threaded with carbon nanotubes (CNTs) were synthesized via a simple solution-phase method, where the Birch reduction chemistry was introduced for the functionalization of CNTs. Selective loading of CuO nanosheets was achieved due to the in situ nucleation and growth of CuO near the functional bands. Finally, discrete CuO nanosheets distributed along the axis direction of CNTs were revealed. The obtained CuO nanosheets exhibited the features of extremely thin thickness, mesoporous structure and high surface area. More importantly, the CNTs go through the inner part of the CuO nanosheets, which ensures the enhanced conductivity for electron transportation. When served as anode materials for lithium ion battery, these CuO/CNT hybrids exhibited much lower charge transfer resistance, in contrast with that of the pure CuO nanosheets. The construction of the necklace-like CuO/CNT hybrids can largely enhance the kinetics performance of the CuO anodes.

Introduction

Attaching functional nanostructures to carbon nanotube (CNT) sidewalls is of interest for targeting CNT hybrid materials with attractive features and promising applications[1-3]. The combination of the two classes of material (functional materials and CNTs) may lead to a successful integration of the properties of the two components that present important feature for biotechnology[4, 5], catalysis[6, 7], and energy storage and conversion[8-11] etc. In recent years, for instance, many efforts have led to the development of oxide/CNT hybrids as anode materials for next-generation lithium ion batteries, which reveals enhanced properties both in high capacity and good cyclic performance[12-15]. Basically, the introduced CNTs in oxide anode can not only buffer the volume changes during Li^+ insertion/extraction but also provide a reliable 3D conductive scaffold for electron transportation. There have been numerous reports of this type of CNT composite anodes. For example, Jeong's group propose a scalable production of CuO/CNT nanocomposites in which each mesoporous oval-shaped CuO particles is threaded with a CNT in the long-axis direction[16]. Such composites exhibited significant advances in the electrochemical performances, including a high reversible capacity (650 mAh g^{-1} at 0.1C), a stable capacity retention, and a high rate capacity (580 mAh g^{-1} at 5C). Similarly, the enhanced electrochemical performances are also demonstrated in other CNT hybrid electrodes, where SnO_2 nanoparticles[17], MnO_2 nanoflakes[18], mesoporous TiO_2[19], Fe_2O_3 nanohorns[20], winterweet-flower-like $CoFe_2O_4$[21], and MoS_2 nanosheets [22]are decorated on CNT sidewalls.

It is of fundamental interest to develop synthetic strategies for controlled loading of oxide materials onto the surfaces of CNTs without disturbing the electrical contacts between the CNTs, so that such materials can be used as high-performance anode materials for lithium ion batteries. However, the optimal construction of oxide/CNT hybrids has been highly challenging, mainly due to the following questions: First, the pristine CNTs hold the inert sidewalls, which always results in hardly dissolving in solvents and/or loading foreign materials. Usually, the surface functional groups introduced via the covalent or noncovalent modification are necessary to get a uniform CNT solution and serve as nucleation centers for loading oxide components[23, 24]. Second, the functionalization location on the CNT surface remains a major challenge due to the lack of control[25]. To date, although massive approaches for the chemical functionalization of CNTs have been reported, most of the functional groups can only be randomly introduced both in covalent and noncovalent modifications. In most cases, the reported hybrid heterostructures refer to the nanoparticles adorned CNTs while the location for foreign component loading is still out of control. Thirdly, the manipulation windows for functional CNT (f-CNT) solution, such as concentration, pH values or solvents, are extremely limited. Therefore, it is difficult to modulate the growth of foreign materials when CNTs were involved. Finally, the interfacial adhesion between the oxide component and CNTs should be enhanced for practical applications. In most cases, the electrostatic interaction is considered as the driving force for bonding the oxide particles onto CNTs. Nevertheless, few works address the question that if the bonding is strong enough for maintaining the conductive statement since the complex charge/discharge processes can easily disturb the electrostatic interaction. To the best of our knowledge, however, the previous attempts had not been fully successful. Most of the works for oxide/CNT hybrid electrodes are individual, which keep claiming the enhanced electrochemical performances rather than reasonable design of oxide/CNT anodes with well-defined structures.

Recently, Wang's group proposed a defect-activated propagation method based on Birch reduction chemistry to decorate the CNTs surface with functional group[26, 27]. This method undergoes a mild chemical treatment process as well as maintains the CNT honeycomb lattice. Furthermore, it can confine the reaction fronts in the tubular direction and obtain a segmented functionalization patterns along the axis of CNTs. These works give the chance to achieve the controllable functionalization of CNTs, which can be used for selectively loading of foreign materials. As expected, by using these unique f-CNTs, a new class of CNT hybrid anodes with beaded-string geometry or necklace-like architecture was achieved, in which the CNTs serve as the thread element and the activated beads are threaded on the CNTs[28-30]. For the further exploration of unique CNT hybrids, herein, the selectively adorned CNTs with mesoporous CuO nanosheets was achieved and the enhanced kinetics performance for lithium storage was also demonstrated.

Experimental

The functionalization of CNTs via Birch reduction chemistry to yield –$(CH_2)_5COOH$ groups decorated f-CNTs was achieved as follows: Firstly, 100ml liquid ammonia was obtained by cooling with the mixture of dry ice and acetone. After that, 50 mg raw multiwall carbon nanotubes and 145 mg sodium was added with continuous magnetic stirring. Then, 6-bromo-hexanoic acid (1.625 g) was added and allowed to react for about 50 minutes. Sodium and 6-bromo-hexanoic acid could be alternatively added for two or three times to get highly functionalized CNTs. Then, the mixture remained stirring overnight until the liquid ammonia evaporated. Finally, the f-CNTs solution was obtained by filtration washing and repeated extractions from hexane using NaOH solution (pH ≈ 11).

The procedure for CuO Nanosheets loading was conducted as follow: 160 μl of $CuCl_2$ solution (1 M) mixed with 160 ul concentrated ammonia solution was diluted with 5 ml deionized water. Then, 5 ml f-CNT solution were added under stirring. The mixture was then maintained at 80 °C for about 2 h. The formed precipitates were harvested by centrifugation and washed thoroughly with deionized water. For comparison, the CuO nanosheets were also synthesized as mentioned above with the absence of CNTs.

The working electrodes were prepared by mixing the CuO/CNT hybrids, carbon black, and binder polyvinylidene fluoride (PVDF) at a mass ratio of 80:10:10. Test cells were assembled in argon filled glove box. Metallic lithium foil was used as counter electrode. The electrolyte was made of 1 M LiPF6 dissolved in the mixture of ethylene carbonate (EC) and diethylene carbonate (DEC) with the volume ratio of 1:1. For EIS measurement, the carbon black is not introduced and the mass ratio for active materials and PVDF is 90:10. The EIS analysis was performed on Ametek VMC-4 electrochemical system between a frequency range of 0.05 Hz ~ 100 kHz.

Results and discussion

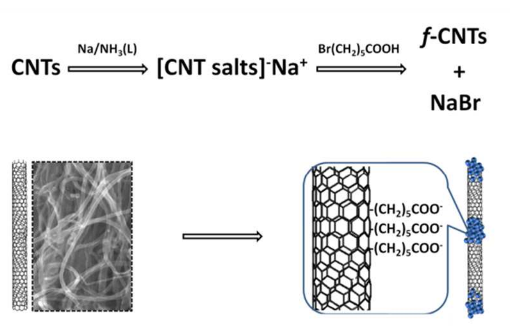

Scheme 1. Schematic illustration for the functionalization of CNTs via Birch reduction chemistry. A segmented functionalization patterns along the axis of CNTs were obtained based on the defect-activated propagation mechanism.

The functionalization of CNTs via the Birch reduction chemistry to yield –$(CH_2)_5COOH$ groups decorated f-CNTs is illustrated in scheme 1. Liquid ammonia is an ionising solvent. It can dissolve the metallic sodium to form a strong reducing agent solution. The solvated electrons add to the CNT surfaces and cause the negative charge of CNTs to form the named $[CNT\ salts]^{-}Na^{+}$ composites[31]. When 6-bromo-hexanoic acid is added, the $(CH_2)_5COOH$ group serves as proton to attach the radical CNT anion with covalent bond, which leads the formation of f-CNTs.

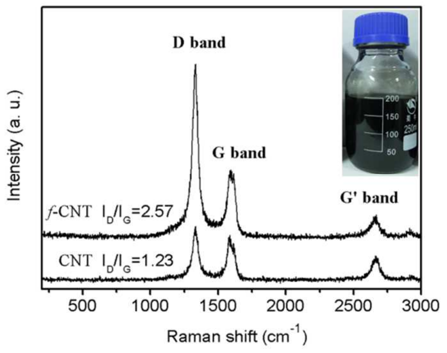

Figure 1. Raman spectra of pristine CNTs and f-CNTs, showing the increased D band after functionalization. Inset is a photograph of f-CNTs dispersions in NaOH solution (pH ≈ 11).

The covalent attachment of alkylcarboxy group can be demonstrated by Raman spectra. As shown in Figure 1, The D band observed at ~1320 cm^{-1} is aroused by the first-order zone boundary phonons, which presents the presence of defects associating with the chemical disruption of the sp^2-hybridized carbon network. The G peak located at ~1580 cm^{-1} and G′ peak at ~ 2700 cm^{-1} are originated by in-plane optical vibrations of sp^2 carbon atoms and second-order zone boundary phonons, respectively[32]. By compared, It is observed that the relative intensity of D band for f-CNTs is much larger than that of pristine CNTs. The increase of I_D/I_G ratio indicates that the sp^2 electrons of CNTs were partly damaged due to the covalently attachment of alkylcarboxyl groups, which is characteristic of the introduction of sp^3-hybridized carbon within the nanotube framework. Similar changes were observed when CNTs were functionalized with 4-carbon-methoxyphenyl[33]. On the other hand, after being functionalized, the f-CNTs can be easily dispersed in basic water (NaOH, pH ≈ 11) due to the hydrophilic nature of carboxyl groups (Figure 1 inset). The obtained f-CNT solution is stable at room temperature, which can be maintained for several weeks without any precipitation.

Recent works reveals that the attachment of the functional groups start at the defect position and propagate along the tubular direction[27]. Thus, the discrete functionalization bands along the axis of CNTs are likely formed (as illustrated in scheme 1). Meanwhile, the obtained f-CNTs are negatively charged due to the electronegative carboxyl groups when they are dispersed in water. Consequently, these functional bands could serve as nucleation centers for the growth of CuO due to the electrostatic interaction between the functional groups and the cations (Cu^{2+} or $Cu(NH_3)_4^{2+}$). The nucleation happened near the functional bands results the selective loading of foreign components while the deposition can hardly be achieved on the raw sidewalls.

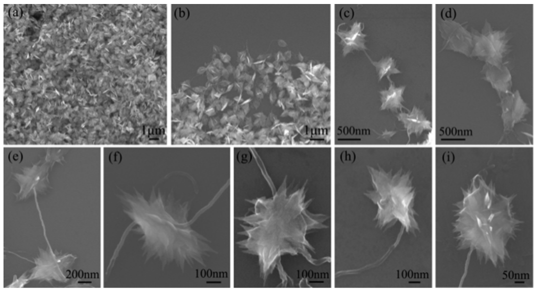

Figure 2. SEM images of the CuO/CNT hybrids in (a), (b) low magnification and (c)-(e) high magnification, showing the necklace-like architecture due to the selective loading. (f)-(i) The individual CuO nanosheets decorated on CNT sidewalls or tips.

Figure 2 shows the SEM images of the CuO/CNT hybrids obtained by a simple and mild solution-phase synthesis. The low magnification images shown in Figure 2(a) and (b) reveal that the CuO nanosheets are formed on a large scale. The size of the CuO nanosheets is estimated to be about 1 μm while the thickness is extremely thin. As expected, it is found that most of the CuO nanosheets are threaded together with the CNTs. Different from the random decorated CNT hybrids, the obtained CuO/CNT hybrids reveal the selective loading of CuO nanosheets along the axis of CNTs. Discrete CuO nanosheets decorate the CNTs and the naked CNT segments can be found simultaneously. Figure 2(c)-(e) shows the necklace-like architecture of the CuO/CNT hybrids. It is obvious that the CNTs go through the inner part of the CuO nanosheets, which prevents the peeling of the CuO nanosheets and ensures good electrical contact. The overall pictures for the joint section of the CuO/CNT hybrids can be found in Figure 2 (f) and (g). In addition, Figure 2 (h) and (i) demonstrated that the loading of CuO nanosheets can also be achieved at the tip area of the CNTs. For Comparison, the control experiments were also carried out in the absent of CNTs while the essential conditions were kept the same. The results were shown in Figure S1, where the individual CuO nanostructures without the CNT strings were obtained. Several nanosheets assembled together to form the hierarchical/flower-like architecture.

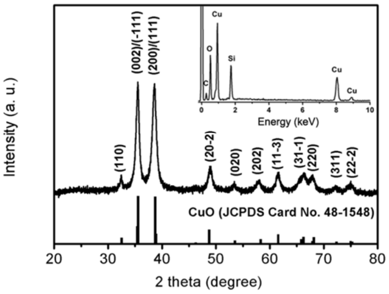

Figure 3. XRD pattern and (inset) EDS analysis of the CuO/CNT hybrids.

Figure 3 shows the XRD pattern of the obtained CuO/CNT hybrids, which indicates that the hybrids consist crystallized CuO. All the diffraction peaks can be indexed to a monoclinic phase of CuO (JCPDS No. 48-1548). Figure 3 inset shows the EDS analysis of the CuO/CNT hybrids, which reveals the presence of C, Si, O and Cu. The Cu and O are dominated while the Si originate from the Si substrates for measurement. Figure S2 shows the TG and DSC curves of the CuO/CNT hybrids in air atmosphere. The mass loss below 285 °C can be attributed to the release of adsorbed species such as alcohol and water. The decomposition of the CNTs starts from 285 °C, which cause the mass loss in the temperature range of 285-700 °C. It is found that the CNTs only account for about 6.5% of the CuO/CNT hybrids.

The major chemical reactions involved for the formation of CuO can be described as follows:

$$Cu(NH_3)_4^{2+} + 2\ OH^- \rightarrow CuO \downarrow + NH_3 + H_2O \qquad (1)$$

Firstly, complex ion: $Cu(NH_3)_4^{2+}$ was formed due to the coordination reaction between Cu^{2+} and excessive ammonia. When the mixture was maintained at 80 °C, the releasing of the NH_3 gas as well as the high temperature would induce the decomposition of $Cu(NH_3)_4^{2+}$ and subsequent formation of CuO clusters. Of course, the CuO clusters likely formed near the functional groups due to the electrostatic interaction. Actually, it is obvious that each CuO nanosheet shows the hierarchical structure, which consists of nanosized subunits, such as nanorods or nanoribbons (Figure 2c-i). Thus, it seems that the aggregate-mediated growth mechanism is much more reasonable for the growth process of CuO nanosheets, which is similar to the other reported CuO nanostructures based on the solution-phase synthesis[34].

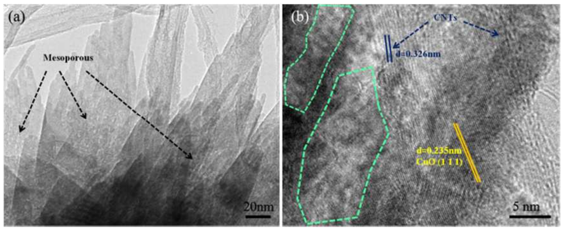

Figure 4. TEM and HRTEM images of the CuO nanosheets. The mesoporous features are revealed. The area marked in (b) shows the vacancies formed at the adjacent area of the rod-like building blocks.

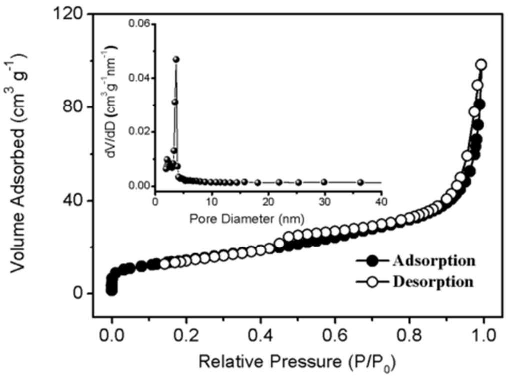

Figure 5. N_2 adsorption‑desorption isotherms of the CuO/CNT hybrids at 77K. The inset is the corresponding pore size distribution.

Figure 4 reveals the TEM images of the CuO/CNT hybrids. The fringe spacing of 0.235 nm represents the spacing of (111) plane of the CuO and the 0.326 nm fringe spacing indicates the interlayer distance of the CNTs (Figure 4b). From the tip areas of the CuO nanosheets, it is found that the final products indeed are built from the nanorods by aggregation along identical directions. Different from the atom-to-atom growth mechanism, the aggregation-mediated growth easily give the chance to form mesoporous structures. As shown in Figure 4(a), the CuO nanosheets exhibit the rough surface, edges and a lot of vacancies can be observed as well. In particular, the mesoporous can be easily formed at the adjacent area due to the irregular shapes and the misorientation of the building blocks (marked area in Figure 4b). The surface area of the CuO/CNT hybrids is further characterized by Brunauer‑Emmett‑Teller (BET) method. Figure 5 exhibits the N_2 adsorption‑desorption isotherms at 77K while the insets show the corresponding pore size distribution. It is found that the CuO/CNT hybrids have a higher BET surface area of 51 m^2 g^{-1}. The presence of mesopores with the size near 3.6 nm is demonstrated.

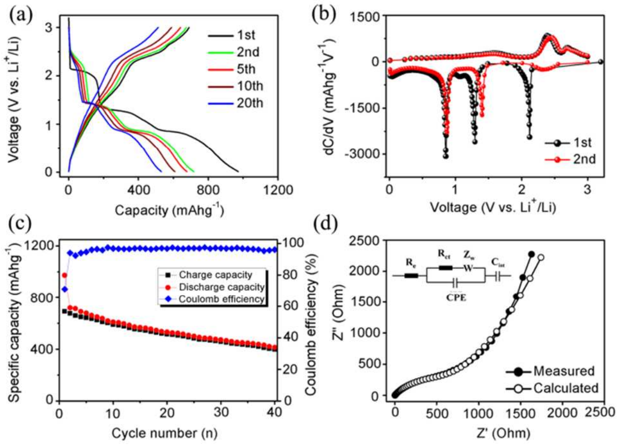

Figure 6. (a) Discharge-charge curves of the CuO/CNT hybrids in the appointed cycles and (b) the differential capacity, dC/dV versus voltage plots extracted from the Discharge-charge curves. (c) the cycle performance and (d) Nyquist plots of the CuO/CNT hybrids.

Basically, the high porosity and extremely thin thickness of the obtained CuO nanosheets allow easy access of Li ions[35, 36]. Meanwhile, the CNTs could provide a 3D matrix with continuous electron transport channel, which ensures the good electronic conductivity for the improved electrochemical performance. Herein, the obtained CuO/CNT hybrids were employed as anode materials for lithium ion batteries and the lithium storage properties were investigated.

Figure 6(a) displays the discharge-charge curves of the CuO/CNT hybrids. The discharge-charge behaviours are corresponding well with the reported CuO anodes. Three discharge plateaus correspond to a multistep electrochemical reaction, which is generally attributed to the formation of an intermediate phase (solid–solution process), the reductive reaction from CuO to Cu_2O and further decomposition to Cu and Li_2O, respectively[37]. Figure 6(b) shows the differential plots, which clearly reveals that these reactions occur near the potentials of 2.12 V, 1.30 V and 0.85V, respectively. For the charge process, the reaction potentials in the range of 2.3 – 2.7 V are recorded, which are ascribed to the oxidation of CuO to Cu_2O and/or CuO. The cyclic voltammogram (CV) curves shown in Figure S3 also reveal the similar mechanism for the CuO anodes, which can be expressed as follows[38, 39]:

$$CuO + 2\,Li^+ + 2\,e^- \leftrightarrow Li_2O + Cu \qquad (2)$$

Figure 6(c) exhibits the cycle performance of the CuO/CNT hybrids. It can be seen that the CuO/CNT hybrids exhibit a high initial discharge capacity of 972 mAh g^{-1} and a reversible capacity of 690 mAh g^{-1}. Then the CuO/CNT hybrids demonstrates a slow capacity fading and shows a capacity above 400 mAh g^{-1} after 40 cycles. The cycle performance is comparable with the former reported CuO nanostructures[40-42]. However, the cycle stability is not good enough, which should be further improved for practical application.

EIS measurements were employed to deeply understand the kinetics performance of the CuO/CNT hybrids. Figure 6(d) shows the Nyquist plots of the fresh prepared CuO/CNT anode from 100 kHz to 0.05 Hz, which is composed of a high-frequency semicircle and a low-frequency line. These impedance results were analyzed by fitting to an equivalent electrical circuit (Figure 6d inset)[43, 44]. The intercept on the Z real axis in the high frequency region corresponds to the R_e while the medium frequency range is related to the R_{ct}. R_e is the ohmic resistance of the electrolyte and R_{ct} is the charge transfer resistance, relating to the charge transfer through the electrode/electrolyte interface. The Warburg impedance (Z_w) is related to the inclined line in the low-frequency region, which represents solid-state diffusion of Li^+ in the electrode materials[45, 46]. For comparison, the pure CuO nanosheets were also characterized and the results were shown in Figure S4. It clearly finds that the R_{ct} of the CuO/CNT hybrids (~756Ω) is much smaller than that of the pure CuO nanosheet electrode (~9.19E4Ω). It should be pointed out that no carbon black was introduced in the electrodes during the EIS measurements. Thus, the CNT plays an important role in making charge transfer much easier, and consequently decreases the internal resistance. Moreover, the inclined line in the low-frequency region is not obvious for the pure CuO nanosheet electrode (Figure S4). It indicates that the electrochemical activity of the pure CuO nanosheets is much lower due to the lack of electrical contact. These results reveal that the introduction of CNTs can largely enhance the kinetics performance of the CuO anodes.

Conclusions

Based on the functional carbon nanotube obtained via the Birch reduction chemistry, we have achieved the selective loading of copper oxide nanosheets on carbon nanotube sidewalls and developed a unique copper oxide/carbon nanotube hybrids with necklace-like architecture. These hybrids show the advantages both in nanoscaled thickness, mesoporous structures, and good electrical contact. As expected, enhanced kinetics performance is demonstrated when they are employed as anode materials for lithium ion batteries. This approach could be extended to design other carbon nanotube hybrids for the applications in catalysis, fuel cells, super-capacitors and lithium ion batteries.

Acknowledgements

This work was supported by National Natural Science Foundation of China (51222104, 51371134) and Fundamental Research Funds for the Central Universities.

Notes and references

[a] MOE Key Laboratory for Nonequilibrium Synthesis and Modulation of Condensed Matter, School of Science, Xi'an Jiaotong University, Xi'an, 710049, China. E-mail: terey@stu.xjtu.edu.cn, yangsen@mail.xjtu.edu.cn
[b] Electronic Materials Research Laboratory, International Center for Dielectric Research, Xi'an Jiaotong University, Xi'an 710049, China.

Electronic Supplementary Information (ESI) available: [SEM images of the CuO nanosheets, TG and DSC results of the CuO/CNT hybrids, CV curves of the CuO/CNT hybrids and the Nyquist plots of the pure CuO nanosheets]. See DOI: 10.1039/b000000x/

1 V. Georgakilas, D. Gournis, V. Tzitzios, L. Pasquato, D. M. Guldi, M. Prato, *J. Mater. Chem.*, 2007, **17**, 2679-2694.

2 X. H. Peng, J. Y. Chen, J. M. Misewich, S. S. Wong, *Chem. Soc. Rev.*, 2009, **38**, 1076-1098.

3 W. D. Zhang, B. Xu, L. C. Jiang, *J. Mater. Chem.*, 2010, **20**, 6383-6391.

4 L. Minati, V. Antonini, M. D. Serra, G. Speranza, *Langmuir*, 2012, **28**, 15900-15906.

5 B. D. Chen, H. Zhang, C. X. Zhai, N. Du, C. Sun, J. W. Xue, D. R. Yang, H. Huang, B. Zhang, Q. P. Xie, Y. L. Wu, *J. Mater. Chem.*, 2010, **20**, 9895-9902.

6 B. Yoon, C. M. Wai, *J. Am. Chem. Soc.*, 2005, **127**, 17174-17175.

7 P. Serp, M. Corrias, P. Kalck, *Appl. Catal. A*, 2003, **253**, 337-358.

8 Z. Chen, V. Augustyn, J. Wen, Y. W. Zhang, M. Q. Shen, B. Dunn, Y. F. Lu, *Adv. Mater.*, 2011, **23**, 791-795.

9 X. M. Liu, Z. D. Huang, S. W. Oh, B. Zhang, P. C. Ma, M. M. F. Yuen, J. Kim, *Compos. Sci. Technol.*, 2012, **72**, 121-144.

10 X. B. Cheng, J. Q. Huang, Q. Zhang, H. J. Peng, M. Q. Zhao, F. Wei, *Nano Energy*, 2014, **4**, 65-72.

11 G. Q. Zhang, H. B. Wu, H. E. Hoster, X. W. Lou, *Energy Environ. Sci.*, 2014, **7**, 302-305.

12 Z. Chen, D. Q. Zhang, X. L. Wang, X. L. Jia, F. Wei, H. X. Li, Y. F. Lu, *Adv. Mater.*, 2012, **24**, 2030-2036.

13 S. J. Ding, J. S. Chen, X. W. Lou, *Adv. Funct. Mater.*, 2011, **21**, 4120-4125.

14 X. Xu, H. Tan, K. Xi, S. J. Ding, D. M. Yu, S. D. Cheng, G. Yang, X. Y. Peng, A. Fakeeh, R. V. Kumar, *Carbon*, 2015, **84**, 491-499.

15 X. Xu, B. T. Dong, S. J. Ding, C. H. Xiao, D. M. Yu, *J. Mater. Chem. A*, 2014, **2**, 13069-13074.

16 S. Ko, J. I. Lee, H. S. Yang, S. Park, U. Jeong, *Adv. Mater.*, 2012, **24**, 4451-4456.

17 Z. H. Wen, Q. Wang, Q. Zhang, J. H. Li, *Adv. Funct. Mater.*, 2007, **17**, 2772-2778.

18 H. Xia, M. O. Lai, L. Lu, *J. Mater. Chem.*, 2010, **20**, 6896-6902.

19 J. Wang, R. Ran, M. O. Tade, Z. P. Shao, *J. Power Sources*, 2014, **254**, 18-28.

20 Z. Y. Wang, D. Y. Luan, S. Madhavi, Y. Hu, X. W. Lou, *Energy Environ. Sci.*, 2012, **5**, 5252-5256.

21 Y. Wang, J. Park, B. Sun, H. Ahn, G. X. Wang, *Chem. Asian J.*, 2012, **7**, 1940-1946.

22 S. J. Ding, J. S. Chen, X. W. lou, *Chem-Eur. J.*, 2011, **17**, 13142-13145.

23 B. I. Kharisov, O. V. Kharissova, H. L. Gutierrez, U. O. Mendez, *Ind. Eng. Chem. Res.*, 2009, **48**, 572-590.

24 D. Tasis, N. Tagmatarchis, V. Georgakilas, M. Prato, *Chem. Eur. J.*, 2003, **9**, 4000-4008.

25 M. S. Raghuveer, A. Kumar, M. J. Frederick, G. P. Louie, P. G. Ganesan, G. Ramanath, *Adv. Mater.*, 2006, **18**, 547-552.

26 Y. Zhang, Y. H. Wang, *J. Phys. Chem. Lett.*, 2011, **2**, 885-888.

27 S. L. Deng, Y. Zhang, A. H. Brozena, M. L. Mayes, P. Banerjee, W. A. Chiou, G. W. Rubloff, G. C. Schatz, Y. H. Wang, *Nature Commun.*, 2011, **2**, 382.

28 C. F. Sun, K. Karki, Z. Jia, H. W. Liao, Y. Zhang, T. Li, Y. Qi, J. Cumings, G. W. Rubloff, Y. H. Wang, *ACS Nano*, 2013, **7**, 2717-2724.

29 Y. Zhang, M. W. Xu, F. Wang, X. P. Song, Y. H. Wang, S. Yang, *J. Phys. Chem. C*, 2013, **117**, 12346-12351.

30 M. W. Xu, F. Wang, Y. Zhang, S. Yang, M. S. Zhao, X. P. Song, *Nanoscale*, 2013, **5**, 8067-8072.

31 Z. Q. Yang, Y. Q. Sun, L. B. Alemany, T. N. Narayanan, W. E. Billups, *J. Am. Chem. Soc.*, 2012, **134**, 18689-18694.

32 M. S. Dresselhaus, A. Jorio, M. Hofmann, G. Dresselhaus, R. Saito, *Nano Lett.*, 2010, **10**, 751-758.

33 J. L. Bahr, J. M. Tour, *J. Mater. Chem.*, 2002, **12**, 1952–1958.

34 J. P. Liu, X. T. Huang, Y. Y. Li, K. M. Sulieman, X. He, F. L. Sun, *Cryst. Growth & Des.*, 2006, **6**, 1690-1696.

35 Z. Y. Wang, F. B. Su, S. Madhavi, X. W. Lou, *Nanoscale*, 2011,**3**,1618-1623.

36 H. B. Wu, J. S. Chen, H. H. Hng, X. W. Lou, *Nanoscale*, 2012, **4**, 2526-2542.

37 A. Debart, L. Dupont, P. Poizot, J. B. Leriche, J. M. Tarascon, *J. Electrochem. Soc.*, 2001, **148**, A1266-A1274.

38 J. Y. Xiang, J. P. Tu, Y. F. Yuan, X. H. Huang, Y. Zhou, L. Zhang, *Electrochem. Commun.*, 2009, **11**, 262-265.

39 M. W. Xu, F. Wang, B. J. Ding, X. P. Song, J. X. Fang, *RSC Adv.*, 2012, **2**, 2240–2243.

40 J. Y. Xiang, J. P. Tu, L. Zhang, Y. Zhou, X. L. Wang, S. J. Shi, *Electrochim. Acta*, 2010, **55**, 1820-1824.

41 S. Y. Gao, S. X. Yang, J. Shu, S. X. Zhang, Z. D. Li, K. Jiang, *J. Phys. Chem. C*, 2008, **112**, 19324–19328.

42 J. Y. Xiang, J. P. Tu, L. Zhang, Y. Zhou, X. L. Wang, S. J. Shi, *J. Power Sources*, 2010, **195**, 313-319.

43 C. F. Zhang, X. Peng, Z. P. Guo, C. B. Cai, Z. X. Chen, D. Wexler, S. Li, H. Liu, *Carbon*, 2012, **50**, 1897-1903.

44 M. V. Reddy, T. Yu, C. H. Sow, Z. X. Shen, C. T. Lim, G. V. S. Rao, B. V. R. Chowdari, *Adv. Funct. Mater.*, 2007, **17**, 2792 – 2799.

45 P. Zhang, J. X. Qiu, Z. F. Zheng, G. Liu, M. Ling, W. Martens, H. H. Wang, H. J. Zhao, S. Q. Zhang, *Electrochim. Acta*, 2013, **104**, 41-47.

46 H. Tang, J. P. Tu, X. Y. Liu, Y. J. Zhang, S. Huang, W. Z. Li, X. L. Wang, C. D. Gu, *J. Mater. Chem. A*, 2014, **2**, 5834–5840